Catalysis Today 418 (2023) 114085

Contents lists available at ScienceDirect

Catalysis Today

journal homepage: www.elsevier.com/locate/cattod

Hydrothermal synthesis and characterization of Cu-MnO_x catalysts for CO oxidation: Effect of Cu:Mn molar ratio on their structure and catalytic activity

Huiyan Pan [a,b,1], Xiaowei Chen [a,e,*,1], Carlos López-Cartes [c], Javier Martínez-López [d], Enqi Bu [a,e], Juan J. Delgado [a,e,*]

[a] Departamento de Ciencia de los Materiales, Ingeniería Metalúrgica y Química Inorgánica, Universidad de Cádiz, Campus Río San Pedro, Puerto Real, Cádiz E-11510, Spain
[b] Henan Key Laboratory of Industrial Microbial Resources and Fermentation Technology, College of Biological and Chemical Engineering, Nanyang Institute of Technology, Nanyang 473004, PR China
[c] Departamento de Química Inorgánica, Universidad de Sevilla, Sevilla, Spain
[d] Departamento de Ciencias de la Tierra, Universidad de Cádiz, Campus Río San Pedro, Puerto Real, Cádiz E-11510, Spain
[e] Instituto Universitario de Investigación en Microscopía Electrónica y Materiales (IMEYMAT), Universidad de Cádiz, Campus Río San Pedro, Puerto Real, Cádiz E-11510, Spain

ARTICLE INFO

Keywords:
Cryptomelane
$Cu_{1.5}Mn_{1.5}O_4$ spinel
CO oxidation
Redox property

ABSTRACT

A comprehensive study was conducted on the synthesis of Cu-MnO_x catalysts using a one-pot hydrothermal method followed by a calcination step. These catalysts were thoroughly characterized using techniques such as X-ray diffraction (XRD), X-ray fluorescence (XRF), N_2 physisorption, X-ray photoelectron spectroscopy (XPS), temperature programmed desorption and reduction (TPD and TPR), and advanced transmission electron microscopy (TEM). The results revealed that the Cu:Mn molar ratio of the precursors, $Cu(NO_3)_2$ and $KMnO_4$, had a significant impact on the crystalline structure and morphology of the synthesized samples. A Cu-doped cryptomelane with a nanorod morphology was observed when the Cu:Mn molar ratio was 0.05. Conversely, a mixture of Cu-doped cryptomelane nanorods, Mn_2O_3, and $Cu_{1.5}Mn_{1.5}O_4$ spinel nanoparticles was formed at molar ratios of 0.1 and 0.25. The catalytic activities of these catalysts for CO oxidation followed the order: 0.25Cu-MnO_x ≈ 0.1Cu-MnO_x > 0.05Cu-MnO_x > cryptomelane. A good correlation was found between the catalytic performance and reducibility of the catalysts under CO atmosphere that can be related to the ability of the samples to activate the CO molecule. The high reducibility of the sample even at room temperature suggest that the CO oxidation over the synthesized Cu-MnO_x catalysts may follow a Mars van Krevelen model.

1. Introduction

Carbon monoxide (CO) is a highly toxic gas that is colorless, odorless, and tasteless. When inhaled, it easily combines with hemoglobin, leading to hypoxic injury, neurological damage, and even fatalities [1]. The petrochemical industry and the incomplete oxidation of carbon-containing compounds are the primary sources of CO emissions. To mitigate its effects, it is important to fully oxidize CO to carbon dioxide using atmospheric oxygen at low temperatures. Moreover, CO oxidation is widely accepted as a model reaction in heterogeneous catalysis due to its simplicity, with only two reactants and one product [1]. Consequently, CO oxidation has been extensively studied over many different catalysts, including Hopcalite, spinels, cryptomelane, perovskites and noble metal catalysts [2].

In 1920, Lamb, Bray, and Frazer made a significant contribution to the field of catalysis with the discovery of a mixture of oxides composed of Cu, Mn, Ag, and Co. This material, known as Hopcalite, was developed as a commercial catalyst for the low-temperature oxidation of carbon monoxide [3]. Several studies have suggested that the active phase of the commercially available Hopcalite catalyst is the $CuMn_2O_4$

* Corresponding authors at: Departamento de Ciencia de los Materiales, Ingeniería Metalúrgica y Química Inorgánica, Universidad de Cádiz, Campus Río San Pedro, Puerto Real, Cádiz E-11510, Spain.
E-mail addresses: xiaowei.chen@uca.es (X. Chen), juanjose.delgado@uca.es (J.J. Delgado).
[1] These authors contributed equally to this work.

https://doi.org/10.1016/j.cattod.2023.114085
Received 25 December 2022; Received in revised form 26 February 2023; Accepted 5 March 2023
Available online 7 March 2023

spinel [4,5]. In spinel oxides with the formula AB_2O_4, the O^{2-} anions occupy a pseudo-cubic close-packed arrangement, with A-site cations occupying 8 of the 64 tetrahedral interstices and B-site cations occupying 16 of the 32 octahedral interstices [6,7]. The flexible valence state of copper (Cu^{+}/Cu^{2+}) and manganese ($Mn^{2+}/Mn^{3+}/Mn^{4+}$) results in a diverse array of copper manganite spinels ($Cu_xMn_{3-x}O_4$), including $Cu_{0.8}Mn_{2.2}O_4$, $CuMn_2O_4$, $Cu_{1.3}Mn_{1.7}O_4$, $Cu_{1.4}Mn_{1.6}O_4$, and $Cu_{1.5}Mn_{1.5}O_4$ [4,8,9]. The general consensus among researchers is that Mn^{3+} and Mn^{4+} cations occupy octahedral sites, with a limited number of Mn^{2+} cations present on both tetrahedral and octahedral sites. Meanwhile, Cu^{+} and/or Cu^{2+} cations primarily occupy tetrahedral sites, with a limited number of Cu^{2+} cations on octahedral sites [8,10]. The catalytic properties of Hopcalite $Cu_xMn_{3-x}O_4$ catalysts for CO oxidation are influenced by a number of factors, including crystallinity, surface area, redox property, and stability, which are dependent on synthesis methods, drying conditions, calcination atmospheres, and temperatures [5,11–13]. Conventional Hopcalite catalysts are usually synthesized by a solid state method using a physical mixture of MnO_2 and CuO oxides, and additional binders and promoters such as Ag_2O [3]. Although alternative synthesis methods, such as co-precipitation from metal nitrate salts, sol-gel, and precipitation by supercritical CO_2, have been reported, the complexity of these procedures has limited their practical application [11,13,19].

Octahedral molecular sieves (OMS-2) have received considerable attention since the 1990 s due to their exceptional catalytic properties in oxidation reactions, such as CO and VOC oxidation [14,15]. Among the OMS-2, cryptomelane, which is a potassium manganese oxide mineral with formula $K(Mn^{4+},Mn^{2+})_8O_{16}$, exhibit excellent catalytic activities for these reactions. It has been shown that doping cryptomelane with cheap transition metals such as Cu, Co, Fe, and Ni and noble metals effectively improves its catalytic properties [15–17,49,50]. Special attention should be given to Cu-doped cryptomelane catalysts because of their particular promising performance in the CO oxidation [15,16,18]. It has been proven that copper can be easily incorporated into the cryptomelane channels by adding a copper precursor in the solution used in the reflux method, which is one of the most common approaches for synthetizing cryptomelane. However, the shortcoming of this method is that only a limited amount of Cu can be incorporated into the cryptomelane structure [14,15]. Copper can also be deposited onto the cryptomelane surface by a simple impregnation method [20]. In this case, CuO was found highly dispersed on the surface of the cryptomelane and it is considered the active phase for the CO oxidation.

In a previous work, we introduced a simple hydrothermal method for synthesizing cryptomelane, using potassium permanganate as the Mn precursor and ethanol as a reducer [21]. In this work, we have adapted that method to obtain a series of Cu-MnO_x samples with different Cu:Mn molar ratios. A detailed macroscopic and microscopic characterization of these catalysts has shown that the Cu:Mn ratio has a dramatic influence on the phase and the morphology of the sample. Furthermore, the addition of copper also improved the reducibility of the sample under CO atmosphere and enhanced the catalytic activities for carbon monoxide oxidation.

2. Experimental

2.1. Catalyst preparation

The preparation of the cryptomelane sample via hydrothermal method using potassium permanganate ($KMnO_4$ >99 %, Scharlau) aqueous solution and absolute ethanol (CH_3CH_2OH>99.98 %, VWR) was based on our previous work [21]. 50 mL of potassium permanganate aqueous solution (10 g/L) was poured into the Teflon liner vessels of 150 mL and 5 mL absolute ethanol with concentration of 1550 mmol/L was dropwise added to it. The solution occupied approximately one-third of the total volume of the vessels. The homemade six-port autoclave [21] was then sealed and heated to 100 °C with a heating rate of 10 °C/min and maintained at this temperature for 12 h, with a rotation speed of 50 rpm. After cooling to room temperature, the samples were filtered, washed with 50 mL of milliQ water, and dried at 70 °C overnight. The samples were subsequently calcined at 350 °C and 500 °C for 6 h in a muffle oven. The final solid samples were ground manually using an agate mortar and sieved through a 100 mesh sieve. All the dryings and calcinations were performed in static air. The same procedure was used for the synthesis of the Cu-MnO_x samples, but in this case the adequate amount of copper nitrate ($Cu(NO_3)_2{\cdot}3H_2O$ > 99.5 %, Scharlau) was added to the aqueous potassium permanganate solution to obtain the desired Cu:Mn molar ratios (0.05, 0.1, and 0.25). The samples prepared with different Cu:Mn molar ratios were designated as yCu-MnO_x, where y is the molar ratio.

2.2. Catalyst characterization

The specific surface areas of the catalysts were calculated by applying the Brunauer-Emmet-Teller (BET) method to nitrogen adsorption isotherms obtained at − 196 °C on an autosorb iQ3 instrument from Quantachrome Instruments. XRF was used to analyze the metal composition of the catalysts using a spectrometer energy dispersive system M4 Tornado (Bruker). Pressed pellets of the samples were prepared with a stainless steel pellet die (Specac) for the XRF analysis.

XRD measurements were carried out using a D8 Advance-A25 diffractometer (Bruker) with a goniometer radius of 250 mm and equipped with a LynxEye detector, a 0.6 mm divergence slit, a 2.5 primary and secondary Soller slits, and a Ni Kβ filter. Powder samples were placed on a flat amorphous silica sample holder and XRD patterns were collected at room temperature using Cu Kα radiation (λ = 1.5418 Å), a tube voltage of 40 kV, and a tube current of 40 mA. The 2θ range was between 10 and 70 degrees, with a step size of 0.05° and the counting time of 1 s per step. DIFFRAC.EVA V2 software (Bruker) was used for phase identification, while quantitative analysis of the crystal phases present in each sample was carried out using the Rietveld method included in TOPAS V5 software (Bruker).

Samples were characterized by high resolution transmission electron microscopy (HRTEM) and high angle annular dark field scanning transmission electron microscopy (HAADF-STEM) using a Talos F200X instrument. The intensity of the HAADF-STEM signal is roughly proportional to the square of the atomic number (Z^2) of the element being observed. Therefore, it is an effective technique to distinguish small nanoparticles supported on light supports. Elemental mapping was performed using energy dispersive X-ray spectroscopy (EDX) to study the elements distribution at the nanometric scale. The EDX mapping was recorded using a beam current of 200 pA and a dwell time of 128 µs per pixel. The elemental maps were improved for visual quality by applying a Gaussian blur of 0.8 using Velox software. Spatially-resolved EELS analysis was also carried out in STEM mode with a Gatan Imaging Filter (GIF) Continuum accomplished to the Talos microscope. The use of spatially resolved EELS method was deemed appropriate for this study because it reduces the electron induced sample drift and damage. STEM-EELS 2D spectrum image (SI) data were acquired with a 2.5 mm diameter aperture and 0.3 eV/channel energy dispersion, enabling the simultaneous acquisition of the O-K, Mn-$L_{2,3}$ and Cu-$L_{2,3}$ edges. The calculated energy resolution was 1.2 eV. Dual-range EELS (DualEELS™) acquisition mode was used to acquire almost simultaneously both the low-loss and the core-loss. This approach enables the correction of the signal drift in each individual pixel of the SI using the zero loss peak (ZLP). A small amount of characterized dry materials was deposited onto a holey carbon film supported on a 300-mesh nickel grid for TEM studies.

XPS measurements were performed on a SPECS PHOIBOS HSA3500 150 R6 instrument to characterize the surface chemical composition and the oxidation state of the samples. The spectra were collected using Al Kα radiation and an X-ray power of 250 W. The XPS spectrometer was operated in the constant analyzer energy mode, with a pass energy of 40

eV for survey spectra and 35 eV for high resolution spectra. The powder samples were compressed to form self-supported pellets, which were then attached to a double-sided adhesive conducting polymer tape. The binding energy was corrected to the main line of the carbon 1 s spectrum (adventitious carbon) set at 284.8 eV, and the quantitative analysis was performed using CasaXPS software version 2.3.25.

TPD experiments were performed using 75 mg of the sample and a U-type quartz reactor. Before entering the reactor, the gas was passed through a cold trap at − 80 ºC to eliminate H_2O vapor. To remove adsorbed water and carbonates on the samples, the manganese oxide samples were first heated up to 500 °C in a flow of 5 % O_2/He for 1 h. After cooling to room temperature, pure He was flowed into the reactor for another hour. Then, the sample was heated to 900 °C with a rate of 10 °C/min in He. The outlet of the reactor was connected to a mass spectrometer (Thermostar GSD301T1, Pfeiffer Vacuum) to register the product evolution. CO-TPR experiments were performed using the same apparatus as TPD. The sample (75 mg) was first pretreated in a flow of 5 % O_2/He at 500 °C for 1 h. Then, the reactor was cooled down to 125 °C and pure He was introduced into the reactor to remove any physisorbed O_2. The reactor was cooled to room temperature in He and then a flow of 5 % CO/He was introduced and kept flowing 0.5 h at room temperature. Afterwards, the reactor was heated up to 950 ºC and the effluent was analyzed using the same mass spectrometer. Finally, reactor was then heated up to 950 °C and the mass spectrometer was used for the effluent analysis. The total flow rate used in both TPD and CO-TPR experiments was 60 mL/min.

2.3. Catalytic reaction of CO oxidation

Catalytic tests for CO oxidation were conducted using 25 mg of the as-prepared catalyst, which was diluted with 50 mg of SiC, in a U-shape quartz reactor. The catalyst was first pretreated in a flow of 5 % O_2/He (60 mL/min) at 500 °C for 1 h to remove any physisorbed H_2O and CO_2. Subsequently, pure He (60 mL/min) was introduced into the reactor and it was cooled down to room temperature. At this point, and thanks to a flexible nylon 1/8 in. tube, the reactor was taken out from the furnace and placed in a liquid bath (Lauda Proline RP845). The temperature of the bath is set at 20 ºC and the reactor was purged with He for 1 h. Next, the reaction mixture with a total flow rate of 100 mL/min and a composition of: 1 vol% CO, 0.6 vol% O_2 and 98.4 vol% was introduce into the reactor and maintained at this temperature for 30 min. Afterwards, the temperature was increased to 30, 50, 75, 100, 125 and 150 °C with a heating rate of 2.5 °C/min and held for 30 min at each temperature using the liquid bath. The experiments at 175, 200, 225, and 250 ºC were carried out using the tubular furnace due to the temperature limit of the liquid bath. The composition of the gas mixture from the reactor outlet was analyzed by a Bruker CP450 gas chromatograph (GC) equipped with a thermal conductivity detector and equipped with Hayesep A (80/100 mesh) and molsieve (13 × 8/100 mesh) columns.

3. Results and discussion

3.1. Characterization of the catalysts

The composition of the Cu-MnO_x catalysts was analyzed using XRF and the results are presented in Table 1. The obtained Cu:Mn molar ratios of the catalysts (0.06, 0.12, and 0.29) are in close agreement with the nominal values (0.05, 0.1, and 0.25). In pure cryptomelane, the potassium content in the total metal amount (K+Mn) is 13.2 mol.%, which is comparable to the results obtained in previous work using the same synthesis conditions (i.e., temperature and concentrations of $KMnO_4$ and ethanol) [21]. However, as the amount of $Cu(NO_3)_2$ was increased in the synthesis mixture, the potassium content in the total metal amount (K+Mn+Cu) decreased, reaching a low of 0.3 %.

Fig. 1 and S1 show the XRD patterns, Rietveld refinement and quantitative phase analysis of the cryptomelane and Cu-MnO_x catalysts calcined at 500 °C. Without Cu addition to the synthesis mixture, pure tetragonal cryptomelane phase (PDF 44-1386) was obtained as expected. This result is in agreement with previous studies by Chen et al., who reported that OMS-2 is stable up to 600 °C in an O_2 atmosphere [22]. According to our XRD results, the average crystalline size of the obtained pure cryptomelane was 9.3 nm. When Cu:Mn molar ratio was 0.05, the main phase is still cryptomelane (94 %), but a new diffraction peak at 33.2 ° appears, which can be attributed to bixbyite Mn_2O_3 (PDF 71-0636) and was found to be present at 5 % in the sample. No Cu, Cu_2O or CuO diffraction peak is observed on this sample, although the Rietveld analysis considered that 1 % of the sample was $Cu_{1.5}Mn_{1.5}O_4$ phase (PDF 70-0262). It is important to note that K and Cu are elements in the same period of the periodic table, and therefore the effective ionic radius

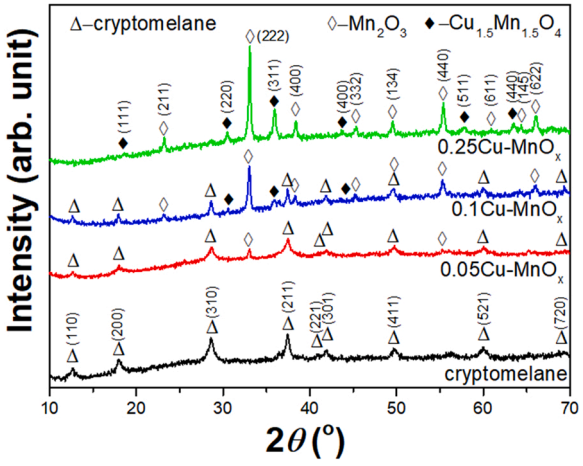

Fig. 1. XRD patterns of pure cryptomelane and Cu-MnO_x catalysts.

Table 1
Textural and compositional properties of pure cryptomelane and Cu-MnO_x catalysts.

Sample	S_{BET}[a] (m^2/g)	Average pore diameter[a] (nm)	Total pore volume[a] (cm^3/g)	Metal composition[b] (mol.%)				Phase composition and average crystalline size[c] (nm)		
				K	Mn	Cu	Cu:Mn ratio	Cryptomelane	$Cu_{1.5}Mn_{1.5}O_4$	Mn_2O_3
cryptomelane	61	18	0.27	13.2	86.8	-	-	100 % (9.3 nm)	-	-
0.05Cu-MnO_x	65	18	0.30	6.0	88.8	5.1	0.06	94 % (7.3 nm)	1 % (66.9 nm)	5 % (52.3 nm)
0.1Cu-MnO_x	41	15	0.15	4.1	85.6	10.3	0.12	41 % (33.3 nm)	9 % (22.0 nm)	50 % (38.2 nm)
0.25Cu-MnO_x	41	14	0.15	0.3	77.3	22.4	0.29	4 % (74.8 nm)	28 % (22.8 nm)	68 % (41.3 nm)

[a] These data were obtained using N_2 physisorption.
[b] Metal compositions of the catalysts were measured by XRF.
[c] Phase composition and average crystalline size of the catalysts were analyzed by Rietveld refinement of XRD patterns.

of K^+ (1.38 Å) is bigger than that of Cu^{2+} (0.73 Å) [23]. The XRF results indicated that this sample contained 6.0 mol.% of K and 5.1 mol.% Cu, and the lower K content in this sample compared to the pure cryptomelane suggests that a certain amount of Cu^{2+} could partially substitute K^+ in 2 x 2 channels to maintain the charge balance in cryptomelane KMn_8O_{16}. Since the discovery of OMS-2 by the Suibś group in 1990 s [24], the incorporation of copper into cryptomelane has been intensively studied. According to the literature, the sol-gel method leaded to formation of CuO on OMS-2, while the reflux method has been used to incorporate small amounts of Cu (≤0.0334 wt%) into OMS-2 [15]. The same research group was able to increase the doping amount of multiple elements (Cu, Mo, V, and Fe) to 10 wt% (each element at 2.5 wt%) using a reflux method without the calcination step. As a result, a pure OMS-2 crystalline structure was obtained [25]. They claimed that Cu^{2+} cations are bigger than Mn^{3+} and Mn^{4+} cations, and that the copper cations are exchanged with Mn^{4+} in the framework of cryptomelane. Kumar et al. prepared 0.292 % Cu-OMS-2 nanofibers and reported that the Cu^{2+} cations are located both in the channels and framework of Cu-OMS-2 [26]. Awaluddin et al. successfully synthesized Cu-doped cryptomelane with higher Cu:Mn molar ratios of 0.01, 0.05 and 0.1 using a sol-gel method with glucose addition [27]. The authors believed that when Cu was added during synthesis, the Cu^{2+} cations initially substituted for Mn ions in the framework, and then began to replace some K^+ ions in the channel sites [27]. In the case of the 0.05Cu-MnO_x sample, compared to the pure cryptomelane sample, the concentration of Mn slightly increased from 86.8 to 88.8 mol.% while the K concentration or the sum of K and Cu elements decreased from 13.2 to 11.2 mol.%. This result suggests that Cu species mostly substitute K^+ cations in the channels of cryptomelane and may also replace a small amount of Mn^{3+} and Mn^{4+} in the framework of cryptomelane. This is reasonable considering that the effective charge radii of Cu^{2+} (0.73 Å) with a coordination number of 6 is smaller than that of K^+ (1.38 Å) and bigger than that for Mn^{3+} (0.65 Å) and Mn^{4+} (0.53 Å) cations [23].

When the Cu:Mn ratio was increased to 0.1, the amount of cryptomelane (41 %) decreases and the amount of Mn_2O_3 (50 %) increases, as shown in Table 1 and Fig. S1. Additionally, a new phase, $Cu_{1.5}Mn_{1.5}O_4$ (PDF 70-0262), was identified thanks to the appearance of a broad diffraction peak at 36 °. The Rietveld analysis showed that it was around 9 % of the sample. The Suibś group reported that Cu doped OMS-2 is stable up to about 450 °C in air [25]. However, they did not assign the new phases formed after calcination at 550 °C. Jothiramalingam et al. synthesized Cu-OMS-2 with a Cu:Mn ratio ranging from 0.10 to 0.13 using an ion exchange method combined with a hydrothermal treatment [28]. They observed that Cu-OMS-2 decomposed into Mn_2O_3 at 480 °C because of collapse of channel structure of cryptomelane, but did not mention what was the new phase of Cu-containing product [28]. All these results suggest that the presence of Cu cations in cryptomelane might promote the collapse of cryptomelane channel structure into the bixbyite Mn_2O_3 phase at a lower temperature than pure cryptomelane.

Similar to Cu:Mn molar ratio of 0.1, the catalyst with Cu:Mn molar ratio of 0.25 also contains the same three phases. However, in this case, only 4 % of the sample still maintains cryptomelane crystalline structure, with 68 % being the Mn_2O_3 phase and 28 % being $Cu_{1.5}Mn_{1.5}O_4$ phase. Table 1 also summarizes the average crystalline size of the different phases in all the samples. In general, as the Cu:Mn ratio increases, the crystalline size of the cryptomelane also increases. The average size of the Mn_2O_3 phase in the Cu-containing catalysts range from 38 to 52 nm, while the average size of $Cu_{1.5}Mn_{1.5}O_4$ is around 22 nm for both 0.1Cu-MnO_x and 0.25Cu-MnO_x catalysts.

Fig. S2a shows the N_2 adsorption and desorption isotherms for the four catalysts. The isotherms of these catalysts exhibit a type II pattern, as classified by IUPAC [29] for nonporous or macroporous solids. The hysteresis loops of these catalysts are assigned to a type H3, indicating the presence of the macropores in the samples. BET specific surface areas of these catalysts are listed in Table 1. Compared to cryptomelane, the 0.05Cu-MnO_x catalyst possessed a slightly higher surface area of 65 m^2/g, while cryptomelane had a surface area of 61 m^2/g. These two catalysts have similar average pore diameter of 18 nm and total pore volume of around 0.30 cm^3/g. The BJH pore size distributions of these two catalysts (Fig. S2b) are comparable, with similar profiles featuring two peaks around 2 and 30 nm corresponding to the mesopores, and a peak at approximately 120 nm assigned to the macropores. However, the BET specific surface areas of both 0.1Cu-MnO_x and 0.25Cu-MnO_x catalysts decrease to 41 m^2/g with the same average pore diameter of 15 nm and the same total pore volume of 0.15 cm^3/g. This decrease of the specific surface area is likely due to the formation Mn_2O_3 and $Cu_{1.5}Mn_{1.5}O_4$, which have larger average crystalline sizes as determined by XRD analysis. Both of these catalysts presented a peak in the macropore range, with a maximum around 70–90 nm (Fig. S2b).

Fig. 2 presents STEM-HAADF images and K and Mn maps of pure cryptomelane catalyst. The sample displays a rod-like morphology with nanorods ranging in length from several hundred nm to a few μm. The Mn and K maps (Fig. 2c and d) indicate that these two elements are distributed very homogeneously. EDX analysis (Fig. S3a) shows that there are 13.4 mol% K and 86.6 mol% Mn in whole area of Fig. 2b, which is very close to XRF results obtained in macroscopic scale.

Fig. 3 shows representative STEM-HADDF and HRTEM images as well as K, Mn and Cu maps of 0.05Cu-MnO_x catalyst. Similar to the pure cryptomelane sample, the nanorods are found to be agglomerated into bundles. Mn, K and Cu elements are distributed homogeneously throughout the sample. The selected area in Fig. 3b contains 10 mol% K, 4.2 mol% Cu and 85.8 mol% Mn (Fig. S3b). Additional EDX analyses of several points in this area were also conducted, showing that the concentration of K ranges from 8.9 % to 10.9 %, while that of Cu rages from 3.4 % to 4.9 %, while Mn is from 85.5 % to 86.8 %. This result indicates that both K and Cu are homogeneously distributed in the Cu-doped cryptomelane nanorods. Furthermore, the EDX results at a nanoscale are consistent with the massive analysis of XRF results. The high resolution TEM images in Fig. 3f and g provide further evidence. The lattice spacings parallel to the nanorods are 5 and 7 Å [21], which correspond to the {110} and {200} family of planes of cryptomelane. The digital diffraction pattern (DDP) analysis of the selected area in Fig. 3g shows the typical diffraction pattern corresponding to the [135] axis zone of cryptomelane. All these findings reveal that the incorporation of Cu in cryptomelane does not alter the morphology or distort its crystalline structure, and support the idea that the copper is mainly incorporated into the cryptomelane channels.

Fig. 4a displays a representative STEM-HAADF image of the 0.1Cu-MnO_x catalyst. Two kinds of morphologies have been identified in this sample: nanorods and nanoparticles. As discussed in the XRD section, this sample is a mixture of cryptomelane, Mn_2O_3 and $Cu_{1.5}Mn_{1.5}O_4$ phases. Fig. 4b, c and d are maps of Mn, K and Cu, respectively. K and Mn can be detected in the same areas, however, there is less Cu present on the nanorods. An EDX analysis of the whole area in Fig. 4a showed a composition of 10.7 % K, 8.3 % Cu and 81.0 % Mn, which is slightly different from the XRF results. An EDX analysis performed in one nanorod (point 1) shows that the composition is 13.7 % K, 1.2 % Cu and 85.1 % Mn. On the other hand, the EDX analysis performed at the point 2, which corresponds to a nanoparticle with a different shape, shows a composition of 1 % K, 42 % Cu and 57 % Mn and therefore probably corresponds to a nanoparticle of $Cu_{1.5}Mn_{1.5}O_4$. The lattice spacings of 7 and 6.7 Å, measured in Fig. 4e, can be assigned to the cryptomelane and Mn_2O_3 phases, respectively. The DDP analysis of the selected areas in Fig. 4f and i confirm the existence of the Mn_2O_3 and $Cu_{1.5}Mn_{1.5}O_4$ nanoparticles oriented along the [012] and [001] axis zone, respectively. We can conclude that TEM results indicate that the Cu-doped cryptomelane phase has a nanorod shape, while the Mn_2O_3 and $Cu_{1.5}Mn_{1.5}O_4$ nanoparticles generally have poorly-defined morphologies.

Fig. 5 shows the chemical characterization of the 0.1Cu-MnO_x sample obtained by EDX and EELS techniques on the marked areas in the HAADF-STEM image. The included spectra are the EDX (Fig. 5b) and

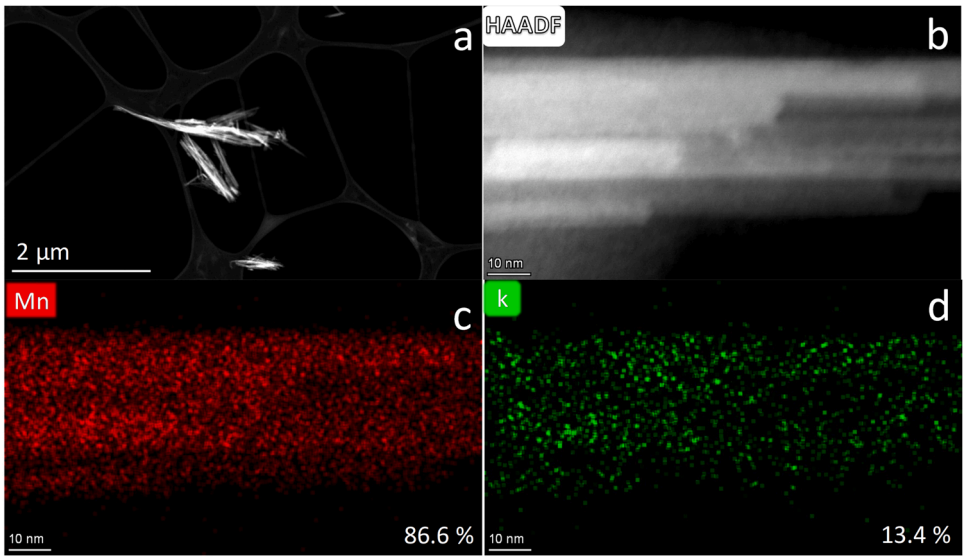

Fig. 2. (a) Low resolution, (b) high resolution STEM-HAADF images, (c) Mn and (d) K maps of pure cryptomelane.

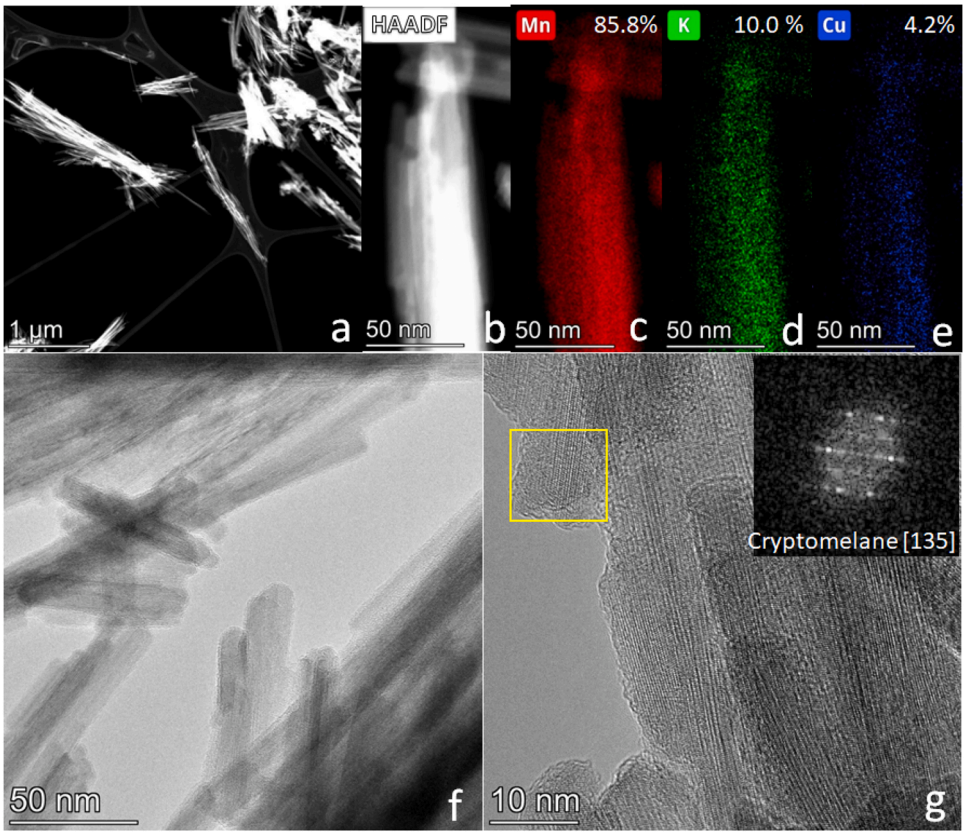

Fig. 3. (a) Low resolution, (b) high resolution STEM-HAADF images, (c) Mn, (d) K (e) Cu maps of 0.05Cu-MnO_x and (f) TEM and (g) high resolution TEM images of 0.05Cu-MnO_x with DDP analysis of selected area.

EELS (Fig. 5c and d) sum spectra of SI experiments. This approach allows to obtain good quality spectra by using a small electron beam dose and dwell time, reducing the electron beam damage to the sample. The EDX spectra of the blue area indicates the presence of Mn and Cu, while the green area also includes K. It should be pointed out that the phase identification based on HREM images of particles in the blue region indicates that those nanoparticles are α-Mn_2O_3 (Fig. 4f), while the nanorods in the green area shows the characteristics channels of the cryptomelane. These results suggest that both the cryptomelane and the bixbyite Mn_2O_3 contain Cu cations. In fact, the Cu:Mn ratio is approximately 0.11 in both areas, which is in good concordance with the values reported by XRF in Table 1. The K content of the cryptomelane is around 10.1 %, which is also in agreement with the XRF results considering the cryptomelane phase content of the sample (41 %). Fig. 5c displays the oxygen K-edge spectra from both areas after background subtraction and reveals two main peaks. The first one (a) is commonly attributed in the

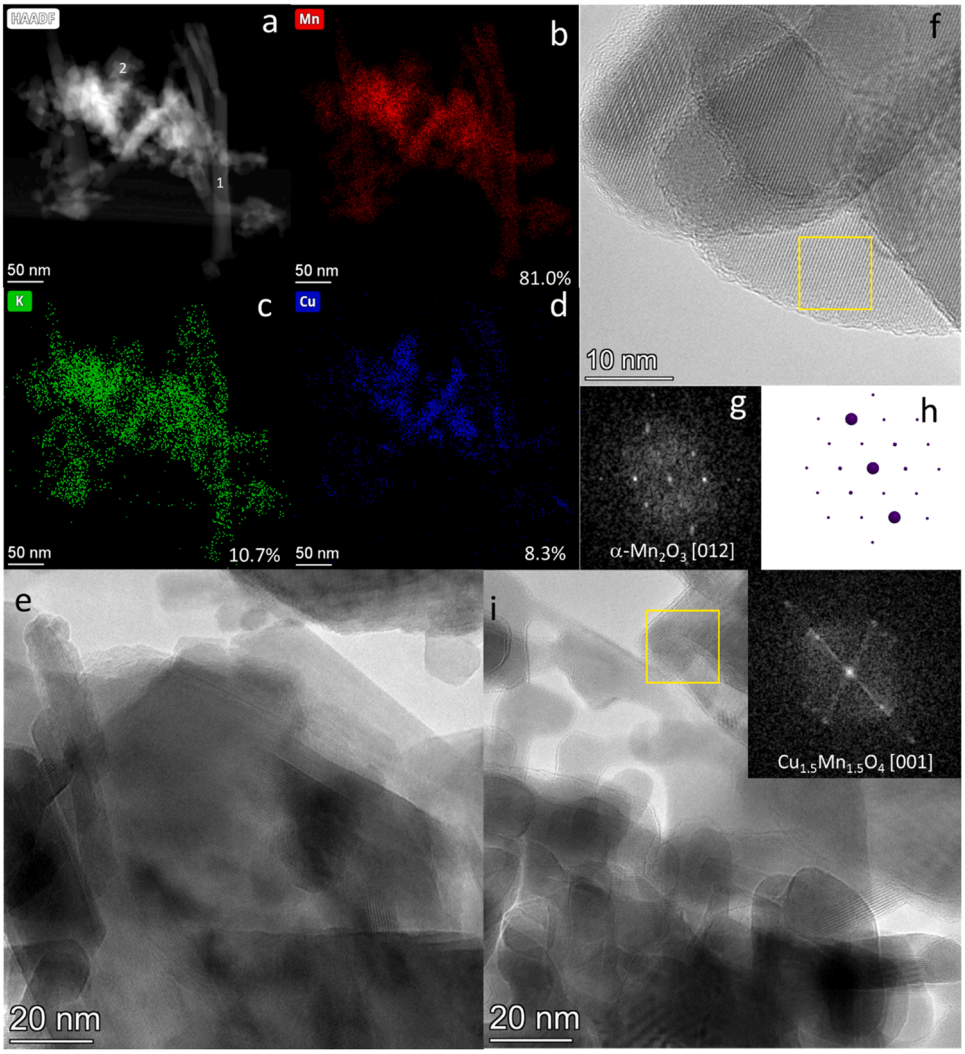

Fig. 4. (a) STEM-HAADF image, (b) Mn, (c) K, (d) Cu maps of 0.1Cu-MnO_x. (e), (f) high resolution TEM images of 0.1Cu-MnO_x (g) DDP analysis of selected area in image f, (h) simulation of diffraction pattern of Mn_2O_3. (i) high resolution TEM image of 0.1Cu-MnO_x with DDP analysis of selected area.

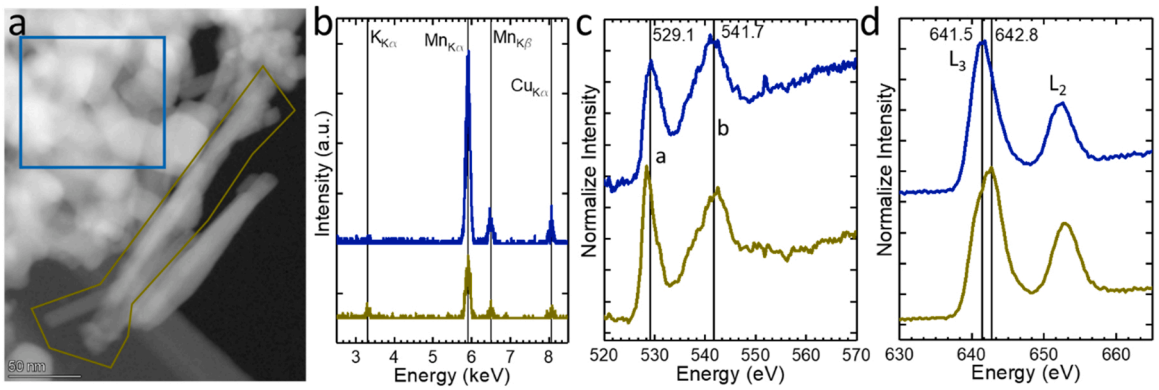

Fig. 5. (a) HAADF-STEM image of sample 0.1Cu-MnO_x with marked areas where EDX (b) and EELS (c: O-K and d: Mn-$L_{2,3}$ edges) experiments were performed.

literature to transitions from 1 *s* to 2*p* states, being the later hybridized with manganese 3*d* orbital. Therefore, this peak is affected by the oxidation state of manganese and it is considered that the peak is higher when Mn 3*d* orbitals have fewer electrons, which means a higher oxidation state [30,31]. The origin of the second peak (b) is assigned to the projected unoccupied oxygen *p* states mixed with the manganese 4*sp* band. Interestingly, the (a) peak is higher than the (b) peak in the case of the spectra obtained in the nanorod, what indicates a high oxidation state of manganese. Additionally, it can be observed that the positions of the peaks slightly change and that the ΔE between them increases in the green spectrum. Both results are similar to those previously reported in the literature for MnO_2 and cryptomelane, while the fine structure of the blue spectrum is in good agreement with those informed for Mn_2O_3 [30, 32].

Fig. 5d includes the manganese $L_{2,3}$-edge spectrum after background subtraction of 0.1Cu-MnO_x. The two white lines, L_3 and L_2, correspond to the excitation of electrons from the $2p_{3/2}$ and $2p_{1/2}$ core states to the unoccupied 3d states of manganese cations. Previous studies have concluded that the position of the L_3 peak shifts to higher energy values with an increase in the formal oxidation state of manganese cations. In the green spectra of Fig. 5d, which corresponds to a cryptomelane nanorod, the maximum is located at approximately 642.8 eV, which is 1.3 eV higher than the L_3 peak of the Mn_2O_3 nanoparticle (blue spectrum). This result is consistent with previous studies of cryptomelane and MnO_2 reported by Zhang and Colliex [30,32]. The shoulder at lower energy values observed for the cryptomelane sample has also been previously reported. Garvie and Craven considered that the undistorted octahedral coordination of Mn^{4+} leads to the split of the *d*-orbital into a lower ($t_{2\,g}$) and higher (e_g) energy levels [33]. They reported that energy split is around 2.0 eV, which is slightly higher than the one found in our study. This may be due to the presence of Mn^{3+}, which would slightly shift the energy to higher values. The authors asserted that the energy split also occurs in Mn_2O_3 but the energy difference is approximately 0.5 eV, which is smaller than the resolution of the experiments and therefore cannot be observed in the blue spectra.

Fig. 6 shows low and high resolution STEM-HAADF images and Mn,

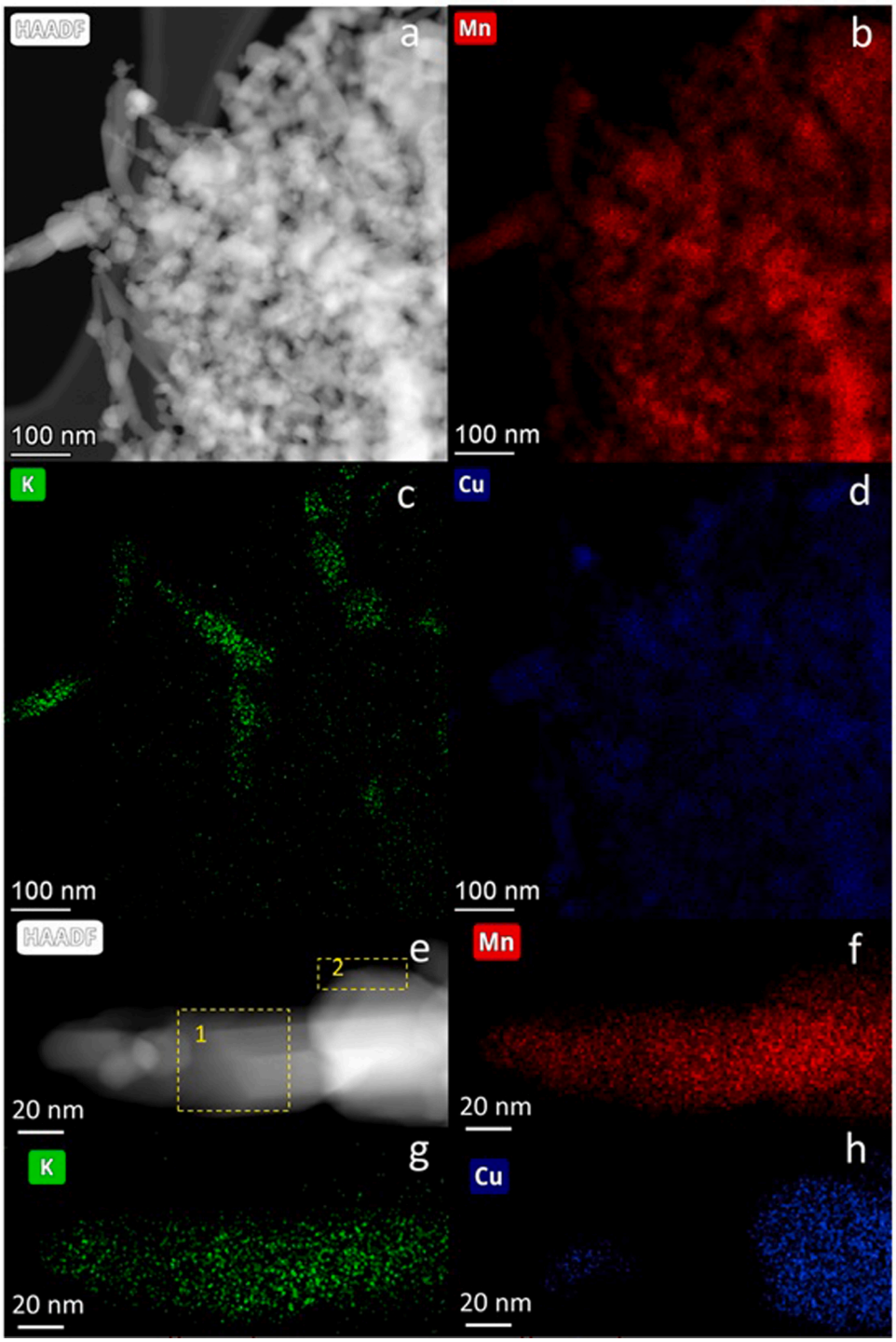

Fig. 6. (a) Low resolution STEM-HAADF image, (b) Mn, (c) K, (d) Cu maps, (e) high resolution STEM-HAADF image, (f) Mn, (g) K, (h) Cu maps of 0.25Cu-MnO_x.

K and Cu maps of 0.25Cu-MnO_x catalyst. Similar to the 0.1Cu-MnO_x sample, this one is also a mixture of nanorods and nanoparticles without specific morphology. Cu and Mn are found in most regions, whereas K is mostly observed in the nanorods, which are cryptomelane with high content of K and low content of Cu. Fig. S3c and d display the EDX spectra of two different areas, showing the notable difference in composition. In area 1, which according to the morphology should be Cu-doped cryptomelane, only 0.2 % Cu and a much higher concentration of K (4.6 %) are detected. In area 2, the contents of Mn and Cu are roughly equal, and the K concentration is much lower (0.6 %). The O:Mn and O:Cu molar ratios are 3:1 in this area and it may correspond to $Cu_{1.5}Mn_{1.5}O_4$ phase, with theoretical O:Mn and O:Cu molar ratios of 2.7. The high-resolution TEM images of this sample (Fig. 7a and b), analyzed using DDP, confirm the coexistence of Mn_2O_3 and $Cu_{1.5}Mn_{1.5}O_4$ phases in nanoparticle morphologies.

Sample 0.25Cu-MnO_x was also characterized by EELS to gain information about the oxidation states of Mn and Cu. These results, as well as the EDX element mapping of the studied area, are included in Fig. 8. Most of the Cu is located in the area marked with a red square, which has a Cu:Mn ratio of 1:1 approximately. This composition would correspond to the $Cu_{1.5}Mn_{1.5}O_4$ phase and the HRTEM analysis of this particle (Fig. 7b) corroborated it. An average Cu:Mn ratio close to 0.12 was found in the nanoparticles included in the blue square that the HRTEM analysis indicates (Fig. 7a) that corresponds to Mn_2O_3. These results probably indicate that the copper incorporation into the bixbyite has reached its maximum value. The analysis of the white lines of Mn obtained by EELS (Fig. 8e) demonstrates that the particles located in the blue square exhibit a similar shape and position as the ones above discussed for the Mn_2O_3 particles of sample 0.1Cu-MnO_x. In the case of the $Cu_{1.5}Mn_{1.5}O_4$, the spectrum is between that observed for cryptomelane (mostly Mn^{4+}) and that observed for Mn_2O_3 (Mn^{3+}), which indicates the co-existence of manganese in both oxidation states. To determine the oxidation state of the copper in each phase, the Cu-$L_{2,3}$ edge was obtained in both areas. In Fig. 8 f, the blue spectrum has two peaks, being the first one higher and located at around 930.9 eV. In a similar manner to what happened in the case of manganese, the first peak can be attributed to electron transitions from the 2*p* core-state to unoccupied *d*-states. Therefore, the intensity of the L_3 peak is directly related to the number of empty states in the *d*-band and increases as the oxidation state increases. In fact, previous results reported in the literature indicate that the metallic copper, which electronic configuration is [Ar] $3d^1$ °4 s^1 and has full 3*d* band, only exhibit a very subtle change at this position [34]. The authors also show that even though the Cu^+ also has fully filled 3*d* orbitals, the L_3 is smaller than the maximum of the L_2. Therefore, the

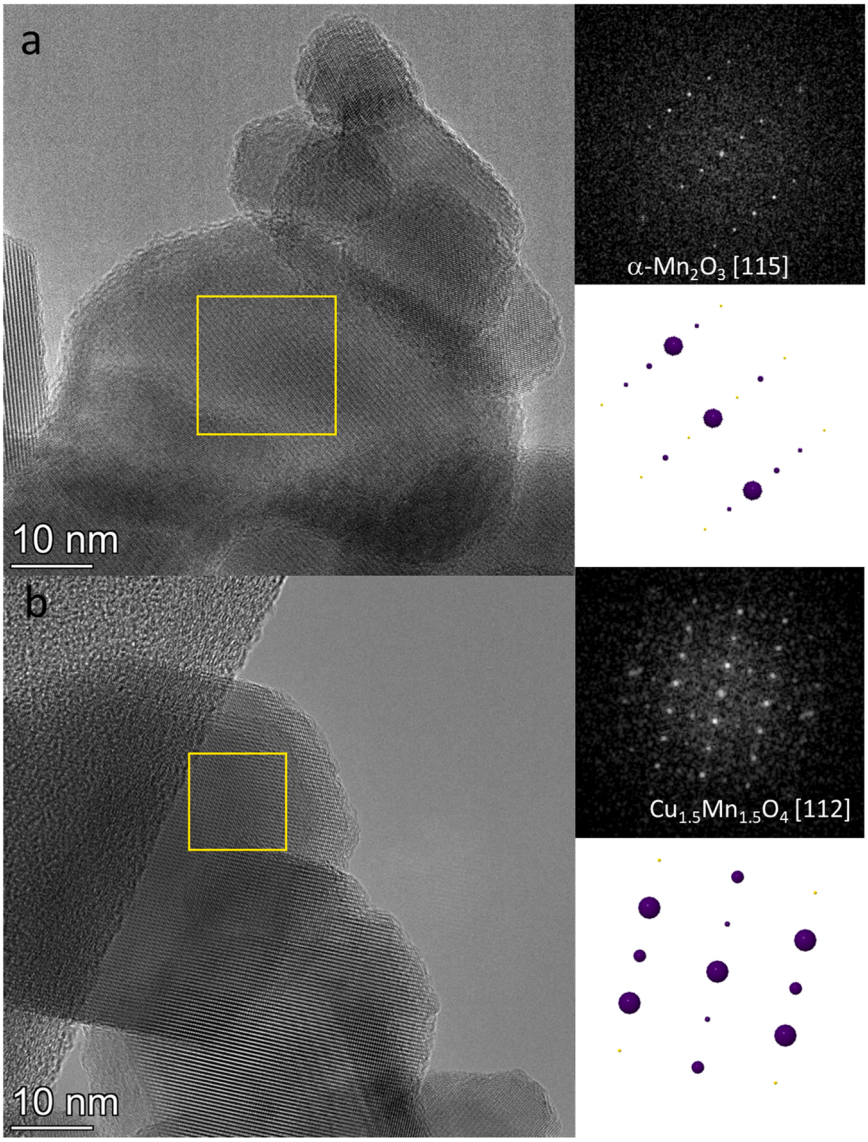

Fig. 7. HRTEM images of 0.25Cu-MnO_x catalyst, DDP analysis of selected areas and simulation of diffraction pattern.

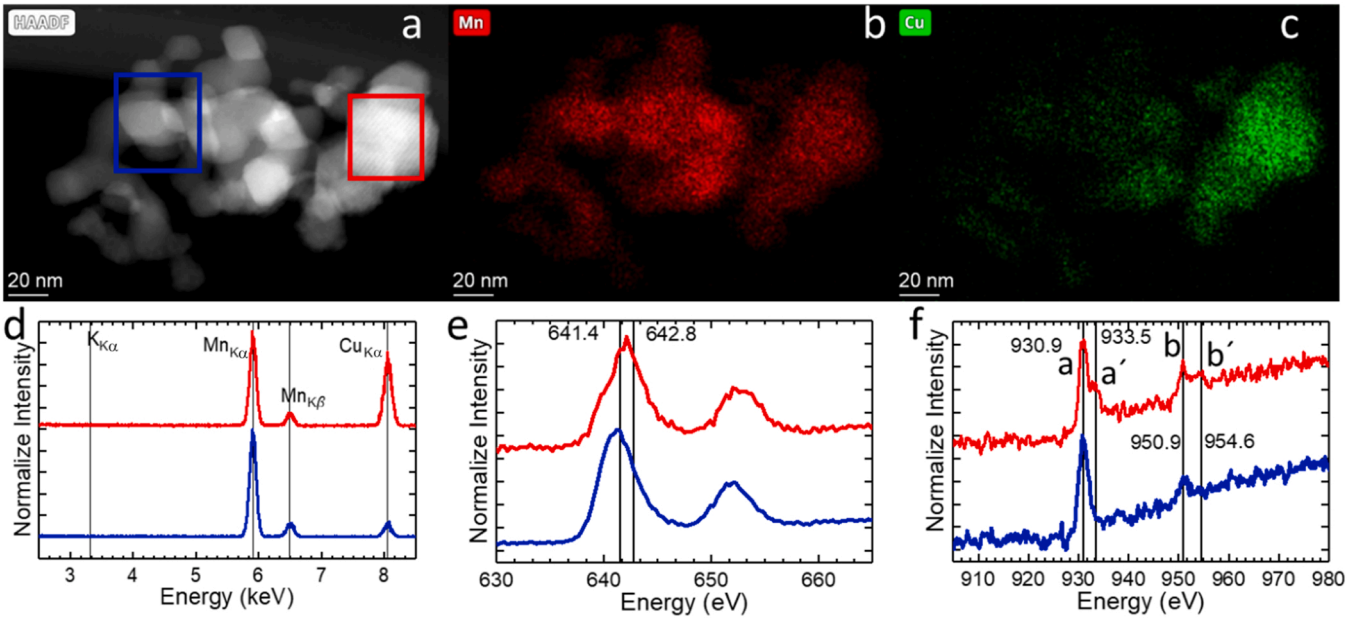

Fig. 8. (a-c) STEM-HAADF and EDX elemental mapping and the (d) EDX, (e) Mn-$L_{2,3}$ edge and (f) Cu-$L_{2,3}$ of the marked areas. The color of the spectra is related to the studied area.

blue spectra can be univocally interpreted as the corresponding to the Cu^{2+}. In the case of the red spectra, we observe two pairs of peaks with a small shift in the position. Interestingly, the first peak is very intense, while the second one is noticeably smaller. This can be related with the relative content of each type of copper ions, but if we consider the relative intensity a´/b´, we can reach the conclusion that it is really related to the presence of Cu^{+}. Consequently, we can conclude that in the $Cu_{1.5}Mn_{1.5}O_4$ phase coexists Cu^{+} and Cu^{2+}.

Table 2 displays the surface composition results of the samples obtained from XPS spectra analysis. The copper amount at the surface of the samples grows as its nominal composition increases. In fact, the Cu:Mn molar ratios are similar to those obtained by XRF analysis, except for the 0.25Cu-MnO_x sample, whose surface Cu:Mn ratio is much lower than that found in the XRF bulk analysis. Additionally, the potassium contents at the surface of the samples 0.05Cu-MnO_x and 0.1Cu-MnO_x are similar to the obtained for the pure cryptomelane, while it is noticeably smaller in the case of the 0.25Cu-MnO_x. This can be explained if we consider that the potassium is mainly ascribed to the cryptomelane nanorods and that due to their small thickness they have a greater impact on the surface composition analysis than the Mn_2O_3 and $Cu_{1.5}Mn_{1.5}O_4$ phases. In the case of the sample with a higher copper content the superficial K content is still higher than the nominal one, but the low content of cryptomelane phase in this sample dramatically reduce the K content on the surface.

Fig. 9 shows high resolution Cu 2*p*, Cu $2p_{3/2}$, O 1 *s* and Mn 2*p* spectra obtained during the XPS analysis of the samples. The Cu 2p spectra of the Cu-MnO_x sample show two main peaks at 932.4 (Cu $2p_{3/2}$) and 951.9 (Cu $2p_{1/2}$) eV and two strong satellite peaks at 942.4 and 960.1 eV, which according to their position are indicative of the presence of Cu^{2+} species [35]. The spectrum of the sample with the highest copper content (0.25Cu-MnO_x) also shows two sharp peaks marked with asterisk in Fig. 9 at lower energy (2.9 eV) than the corresponding main peak. According to the literature, this fact indicates that copper is also present in the 1+ oxidation state in this sample [35,36]. A deconvolution of the $2p_{3/2}$ signal shows that 18.2 % of the total copper is in the Cu^{+} oxidation state in the 0.25Cu-MnO_x sample, while a similar analysis for the 0.1Cu-MnO_x sample shows that 7.3 % of the total copper is in the Cu^{+} oxidation state. The coexistence of both oxidation states in these samples could be related to the presence of a Cu-Mn_2O_3 mixed oxide and the $Cu_{1.5}Mn_{1.5}O_4$ spinel. These XPS results agree well with the previously discussed EELS results that indicates the presence of Cu^{+} and Cu^{2+} species in the $Cu_{1.5}Mn_{1.5}O_4$ spinel and mainly Cu^{2+} in the nanoparticles of Cu-Mn_2O_3 mixed oxide.

Mn 2*p* spectra do not show any significant differences, apart from a slight shift to lower energies of both $2p_{3/2}$ and $2p_{1/2}$ signals in the samples with higher copper content. This shift could be due to an increase in the presence of Mn^{3+} species forming part of Mn_2O_3 and the mixed oxide with spinel structure [37,38]. No changes in the binding energy for the O 1 *s* XPS spectra are observed for any of the samples. O 1 *s* signal can be mainly explained by two contributions at 529.2 and 530.5 eV associated to lattice and defective oxygen, respectively [35]. High resolution XPS spectra of K 2*p* of all the samples are also shown in Fig. S4. The two peaks at 292.1 and 294.8 eV can be assigned to the $2p_{3/2}$ and $2p_{1/2}$ of K^{+} [37], respectively, and the main difference in the peak intensity can related to the amount of K in the sample.

In order to understand the redox property of the Cu-MnO_x catalyst, which is considered to greatly affect its catalytic activity, TPD and CO-TPR experiments were performed. The oxygen release in the TPD experiments are included in Fig. 10. We can observe that the oxygen profile of sample 0.05Cu-MnO_x is very similar to the cryptomelane sample and two main desorption peaks at 567–588 and 733–758 °C are observed. Those peaks are commonly ascribed to the phase transformation from cryptomelane (α-MnO_2) to Mn_2O_3 and from Mn_2O_3 to Mn_3O_4 [20,21], respectively. This is logic if we consider that according to the XRD results both samples are mainly cryptomelane. The main differences between them is that the temperature of the maximum of the peaks slightly shift to lower values and that the peak at 567–588 °C is more intense in the case of the Cu-doped catalyst. According to this, it

Table 2
Surface compositions of pure cryptomelane and Cu-MnO_x catalysts according to XPS calculation.

Sample	K (mol %)	Mn (mol %)	Cu (mol %)	O (mol. %)	Cu:Mn ratio
cryptomelane	8.7	29.5	-	61.8	-
0.05Cu-MnO_x	8.1	29.2	1.4	61.4	0.05
0.1Cu-MnO_x	8.5	31.6	2.5	57.5	0.08
0.25Cu-MnO_x	3.5	33.7	4.6	58.2	0.14

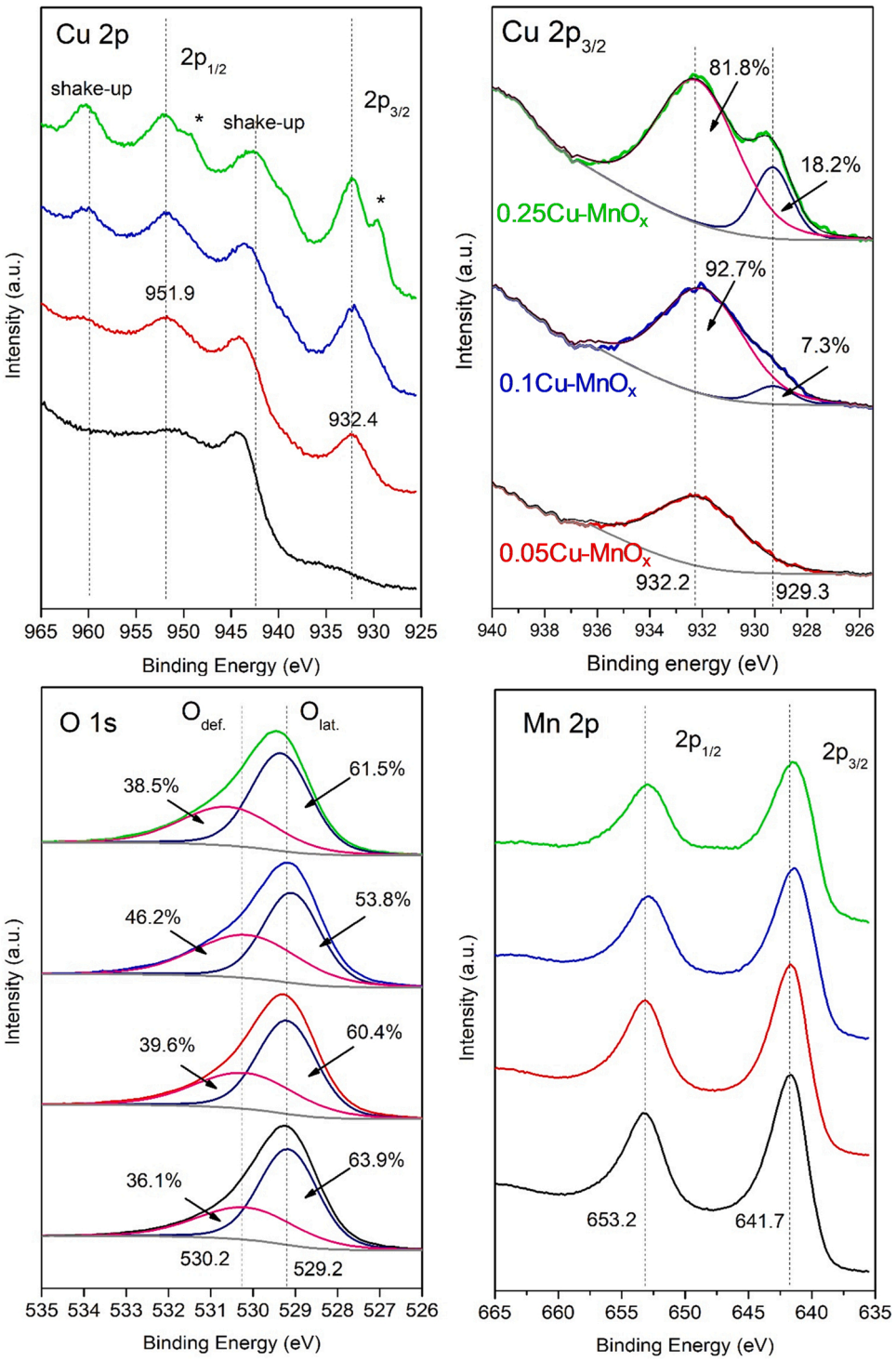

Fig. 9. XPS spectra of Cu 2*p*, Cu 2$p_{3/2}$, O 1*s* and Mn 2*p* of pure cryptomelane (black), 0.05Cu-MnO_x (red), 0.1Cu-MnO_x (blue) and 0.25Cu-MnO_x (green) catalysts.

looks that the presence of the copper promotes the high oxidation state of Mn that it is reduced at lower temperatures (567–588 ºC) and therefore makes the oxygen species more active, which is similar to results described in the literature [14].

The O_2 desorption of the 0.1Cu-MnO_x sample shows three main peaks at around 530, 760 and 796 ºC, with the second peak being the most prominent. XRD analysis suggests that this sample consists mainly of Cu-doped cryptomelane (41 %) and Mn_2O_3 (50 %) with a small amount of $Cu_{1.5}Mn_{1.5}O_4$ (9 %). The O_2 release peak at 530 ºC might be due to superficial Mn^{4+} species of the Cu-doped cryptomelane to Mn_2O_3, while the peak observed at 760 ºC corresponds to the reduction to Mn_3O_4. However, the first peak in this sample is significantly smaller than the second peak when comparing their relative intensities with those observed in the 0.05Cu-MnO_x sample. In fact, the area below the peak at 760 ºC is anomalously high if we consider that only 40 % of the sample is formed of Cu-doped cryptomelane. It should be noted that initially, Cu is incorporated into the cryptomelane channels, and by increasing Cu in the synthesis media, it eventually becomes incorporated into the crystal structure. Therefore, our results may suggest that the incorporation of Cu into the structure improves the thermal stability

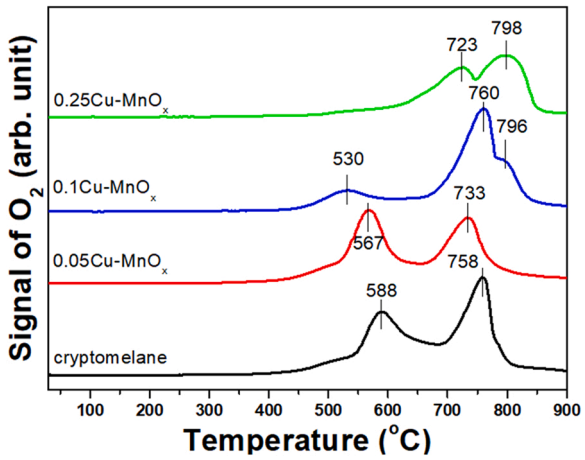

Fig. 10. O_2 release profiles of pure cryptomelane and Cu-MnO_x catalysts during TPD experiments.

of the sample, leading to a reduction of Mn^{4+} species at an even higher temperature. The third peak at 796 °C can be therefore assigned to the phase transformation from the original Cu-Mn_2O_3 phase to Mn_3O_4. The reduction of the $Cu_{1.5}Mn_{1.5}O_4$ phase should also be between both oxygen releases but due to the small contribution in the sample cannot be easily identified [12]. The 0.25Cu-MnO_x catalyst showed O_2 release at 723 and 798 °C, with the latter peak having the largest area. XRD results revealed that the sample was primarily composed of Mn_2O_3 (68 %), $Cu_{1.5}Mn_{1.5}O_4$ (28 %), and a small amount of Cu-doped cryptomelane (4 %). Therefore, both peaks are likely associated with the main phases. The peak at 798 °C can be attributed to the reduction of Cu-doped Mn_2O_3, which is also a main phase in the 0.1Cu-MnO_x sample where a similar peak was observed. This leads us to conclude that the peak at 723 °C is a result of the reduction of the $Cu_{1.5}Mn_{1.5}O_4$ spinel phase.

The catalytic performance of Cu-MnO_x catalysts for CO oxidation is related to the interaction between CO molecules and the active lattice oxygen of the catalysts. Fig. 11a and b show the CO consumption and CO_2 formation profiles during CO-TPR process. The temperatures of CO consumption correspond to the temperatures of CO_2 formation for all catalysts. In the case of the pure cryptomelane catalyst, there are three CO_2 formation peaks at 290, 323 and 407 °C, which have been assigned in literature to the reduction of labile oxygen from cryptomelane to Mn_3O_4 and from Mn_3O_4 to MnO, respectively [39]. Further reduction of MnO to metallic Mn cannot occur even up to 1200 °C due to its large negative value of reduction potential [38]. It has also been reported that cryptomelane can be reduced in three steps [20,40]: cryptomelane (α-MnO_2) → Mn_2O_3→ Mn_3O_4 → MnO. Therefore, the three CO_2 formation peaks over the pure cryptomelane catalyst could be attributed to the three steps of reduction from cryptomelane to MnO.

When the Cu doping amount is 0.05, the three CO_2 desorption peaks of cryptomelane are overlapped and shifted to lower temperatures. The reduction from Cu-doped cryptomelane to Mn_2O_3 is responsible for the appearance of the first peak at 265 °C over the 0.05Cu-MnO_x catalyst, while the second peak at 333 °C is attributed to the transformation from Mn_2O_3 to MnO. This assignment is consistent with literature [12,38]. There is almost no big change of the first CO_2 formation peak at 265 °C when the Cu doping content is increased from 0.05 to 0.1. However, the second CO_2 formation peak of 0.1Cu-MnO_x started to increase at 279 °C, which is lower than those of both pure cryptomelane and 0.05Cu-MnO_x catalysts. The peak is also wider because it is the result of the reduction of the phase mixture present in the sample. It should be pointed out that the phases of this sample are Cu-doped cryptomelane and Mn_2O_3, and it also contains 9 % $Cu_{1.5}Mn_{1.5}O_4$ spinel phase. When Cu:Mn ratio increases to 0.25, both CO_2 release peaks shift to lower temperatures at 255 and 304 °C. As it has been shown in XRD results, the phases of

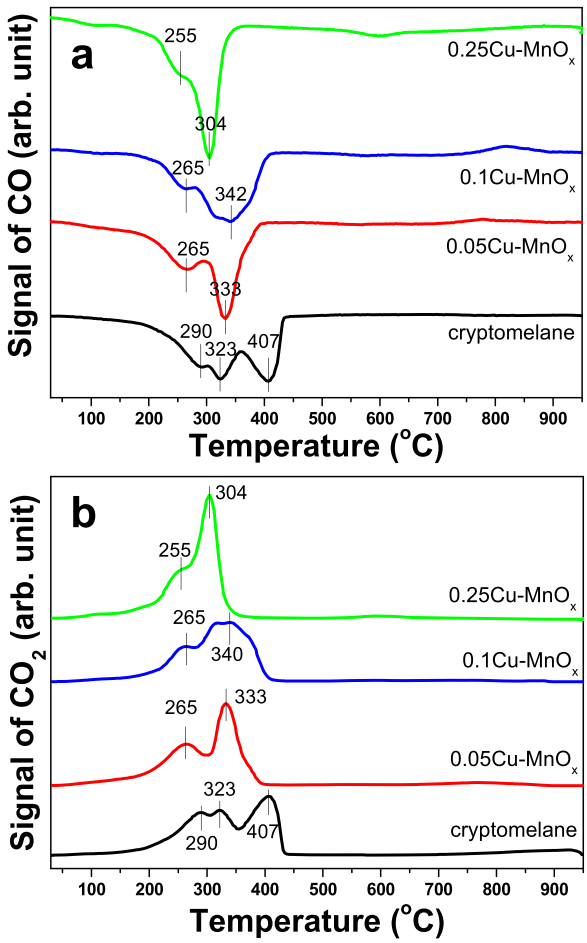

Fig. 11. (a) CO consumption and (b) CO_2 formation over pure cryptomelane and Cu-MnO_x catalysts during CO-TPR experiments.

0.25Cu-MnO_x is dominated by spinel $Cu_{1.5}Mn_{1.5}O_4$ and Cu-doped Mn_2O_3, being the content of the Cu-doped cryptomelane below 4 %. The CO-TPR of pure $Cu_{1.5}Mn_{1.5}O_4$ spinel phase has been reported in the literature to be very similar to the obtained in the case of the 0.25Cu-MnO_x [41]. Therefore, it is expected that the Cu-doped Mn_2O_3 is reduced at the same temperature. Even though, it is commonly accepted that both cryptomelane and Mn_2O_3 are finally reduced to MnO, it is not reported what the reduction process is of the $Cu_{1.5}Mn_{1.5}O_4$. Additionally, the Cu^+ or Cu^{2+} that were detected in the structure of cryptomelane, Mn_2O_3 or the spinel phase by EELS, can be eventually segregated and also be reduced to metallic copper [38,42]. The existence of Cu species on the surface of the sample promote Mn reduction caused by spill-over effect [38] and the reduction peaks thus shift to lower temperature.

3.2. *Catalytic performance for CO oxidation*

The CO conversion of all catalysts for CO oxidation are shown in Fig. 12. CO conversion increases with rising reaction temperatures for all catalysts. Pure cryptomelane catalyst exhibits the lowest CO conversion among the four catalysts. At 250 °C, CO conversion reaches 100 % over pure cryptomelane catalyst, which agrees well with our previous results for cryptomelane calcined at 500 °C [21]. The addition of Cu dramatically improves the catalytic activity, with 100 % CO conversion achieved at 200 °C. Xia et al. reported that Cu-doped OMS-2 with higher Cu concentration presented 100 % CO conversion even at 60 °C under lower space velocity (volume of total gas passed per hour per unit weight) than ours, while only 38.2 % CO was oxidized over Cu-doped

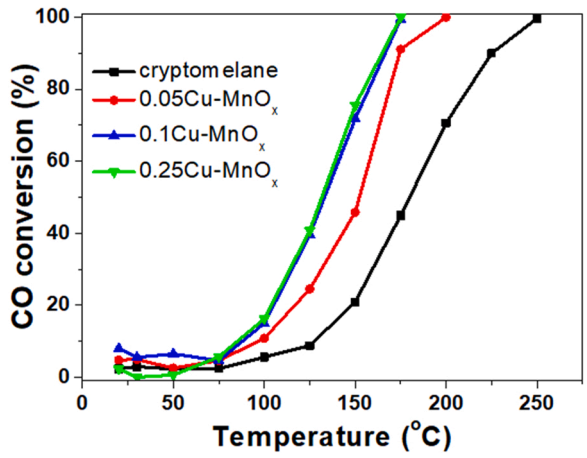

Fig. 12. CO conversion at different temperatures during CO oxidation over pure cryptomelane and Cu-MnO_x catalysts. Total flow rate: 100 mL/min containing 1 vol% CO, 0.6 vol% O_2 and 98.4 vol% He. 25 mg of catalyst mixed with 50 mg of SiC.

OMS-2 with lower Cu concentration [43]. Under these conditions, the undoped OMS-2 catalyst shows no activity towards CO oxidation. This result is in agreement with our findings, although it is difficult to make correlations because the Cu loadings in cryptomelane were not specified. The authors believed that a Cu-O-Mn bridge with appropriate coordination in the OMS-2 structure might be responsible for high activity of Cu-doped OMS-2 catalyst. They suggested that Cu-O-Mn bridge facilitated the reversible electron transfer along the bridge, which may be responsible for the CO oxidation. Additionally, Hernández et al. reported that Cu-doped cryptomelane with a Cu to total metal ratio of 0.042 synthesized by ball milling showed higher catalytic activity for the same catalytic reaction compared to pure cryptomelane [40]. In this case, the authors also consider that CO adsorption on the Cu-doped cryptomelane is higher compared to pure cryptomelane, thanks to the Cu sites. In the present study, XRD results showed that Cu^{2+} species primarily substitute K^+ in the 2 x 2 channels of cryptomelane. As demonstrated in the TPD and CO-TPR results (Fig. 11), the incorporation of Cu cations led to improved oxygen reactivity and reducibility, resulting in an increased catalytic activity for CO oxidation.

The two best catalysts are those with Cu:Mn molar ratios are 0.1 and 0.25 (Fig. 12), and they show similar performances under these reaction conditions. Both catalysts fully oxidize CO at 175 °C. The BET specific surface areas of these two catalysts are similar, but lower than those of the pure and 0.05Cu-doped cryptomelane catalysts. Therefore, we cannot attribute the differences in CO conversions solely to this parameter. In fact, samples with high loadings of copper exhibit even higher intrinsic activity. As previously discussed in XRD section, $Cu_{1.5}Mn_{1.5}O_4$ spinel and Cu-Mn_2O_3 are present when the Cu:Mn ratio is higher than 0.1 (Table 1 and Fig. S1). In fact, the Cu-doped cryptomelane phase is residual (4 %) in the 0.25Cu-MnO_x sample. Therefore, the catalytic improvement may be related to $Cu_{1.5}Mn_{1.5}O_4$ spinel and Cu-Mn_2O_3 phases. In this sense, Ramesh et al. reported that Mn_2O_3 is even more active than MnO_2 for CO oxidation [44]. Hutchings and co-workers studied several copper-manganese mixed oxides obtained by a coprecipitation method and evaluated their catalytic properties using the CO oxidation reaction [4]. The authors found that the most active samples had a Cu:Mn ratio of 1:2, and it was a mixture of $Cu_{1.4}Mn_{1.6}O_4$ spinel and Mn_2O_3. The same research group continued using this method to synthesize Hopcalite catalysts and concluded that the activity of Hopcalite materials is mainly determined by two features: the surface area and the phase composition [45]. The highest activity was observed over the catalyst calcined at 410 °C with high surface area and low crystallinity. They further studied this $CuMnO_x$ catalyst for CO oxidation using temporal analysis of products reactor. A higher contribution of the Mars van Krevelen (MvK) mechanism and a smaller contribution of the Langmuir–Hinshelwood mechanism in the CO oxidation reaction over the $CuMnO_x$ catalyst have been observed [46]. The Mars van Krevelen mechanism involves the following steps:

(1) The metal/support is oxidized in a separate independent step.
(2) CO molecules are adsorbed on the oxide from the gas phase.
(3) Adsorbed CO reacts with surface oxygen atoms from the oxide.
(4) Produced CO_2 desorbs from the surface.
(5) The resulting oxygen vacancies are refilled rapidly and irreversibly by oxygen from the gas phase in a separate step (1).

Liu et al. also reported that the CO oxidation over CuO supported on OMS-2 catalysts follows the Mars van Krevelen mechanism, involving the Cu^{2+}–O^{2-}–Mn^{4+} ↔ Cu^{+}–□–Mn^{3+} + O_2 redox couple [47]. However, Ramesh and his colleagues discussed the CO oxidation mechanism over Mn_2O_3 and MnO_2 catalysts and concluded that the mechanism is either the Langmuir–Hinshelwood mechanism or the Eley–Rideal mechanism [44]. Similarly, Freund et al. claimed that, in general, CO oxidation is a redox reaction and operates in a "simple" Langmuir–Hinshelwood mechanism on the metal catalysts, with some exceptions for noble metals. Therefore, the CO oxidation mechanism over cryptomelane or $CuMnO_x$ spinel is still a topic of debate, despite extensive studies.

In the literature, it is also commonly accepted that the reducibility of the samples strongly determines the catalytic properties [21,48]. This can be the explanation of why the 0.05Cu-MnO_x is more active than the pure cryptomelane, because both TPD and CO-TPD show that the sample with copper release oxygen at lower temperature. Nevertheless, the most two active catalysts (0.1Cu-MnO_x and 0.25Cu-MnO_x) release oxygen at higher temperature in the TPD than the pure cryptomelane and the Cu-doped cryptomelane. Nonetheless, if we consider the CO_2 release during the CO-TPR, we can observe that the reducibility under CO is dramatically improved by the copper incorporation and the samples can be reduced even at room temperature (Fig. S5). This can be related also to the capability of the Cu-doped sample to activate the CO molecule that, as it has previously been reported can be associated to the copper active center on the surface of the catalysts [38,41]. Therefore, it is obvious that the oxygen, probably mainly the superficial one, is available for the Mars van Krevelen mechanism.

Stability tests were carried out using 20 % of oxygen in argon at 125 °C for 24 h. The conversion of CO over different catalysts as a function of time is shown in Fig. 13. We can observe how the CO conversion of all samples was higher when using 20 % of O_2 compared to the tests included in Fig. 12 using 0.6 % of oxygen. This result can be explained

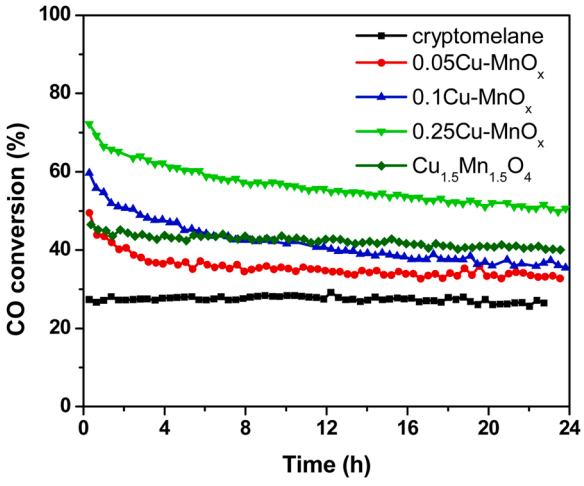

Fig. 13. Stability tests of the catalysts under CO oxidation conditions using 1 % CO and 20 % oxygen in argon at 125 °C during 24 h and a total flow of 100 mL/min. 25 mg of catalyst mixed with 50 mg of SiC was used.

considering the effect of oxygen concentration on the steam in the reaction kinetics and on the redox state of the sample. Pure cryptomelane showed a particularly high increase in activity, with a 1.5-fold increase from 9 % to 25 % conversion. We previously reported that pure cryptomelane can be partially reduced in presence of CO even at low temperatures when low oxygen concentrations are used, leading to low CO conversions. All the studied Cu-doped samples suffer a relatively severe deactivation. In fact, the Cu-doped cryptomelane sample (0.05Cu-MnO_x) showed a higher initial CO conversion than the pure cryptomelane, but due to the deactivation show a final activity near to the pure cryptomelane sample. Due to the complex composition of the samples, we prepared a new material with a 1:1 Cu:Mn ratio using the same synthesis protocol, which according to the XRD results was mainly $Cu_{1.5}Mn_{1.5}O_4$ (Fig. S6). This sample exhibited activity close to double that of cryptomelane but lower than the initial activity observed for the Cu-doped catalysts. Furthermore, its activity remained stable throughout the 24-hour experiment and at the end of the experiment the activity is even higher than that observed for the samples 0.05Cu-MnO_x, 0.1Cu-MnO_x. These results allow us to conclude that the deactivation of the 0.05Cu-MnO_x, 0.1Cu-MnO_x, and 0.25Cu-MnO_x samples is mainly due to the deactivation of Cu-doped cryptomelane and Mn_2O_3.

4. Conclusions

The Cu-MnO_x catalysts with different phase composition and morphology have been successfully synthesized. The main phase is Cu-doped cryptomelane with nanorod morphology when Cu:Mn molar ratio is 0.05. Cu:Mn molar ratios of 0.1 and 0.25 result in a mixture of Cu-doped cryptomelane in nanorod shape and Mn_2O_3 and $Cu_{1.5}Mn_{1.5}O_4$ spinel nanoparticles. The catalytic activities for CO oxidation have been enhanced with incorporation of Cu to cryptomelane crystalline structure and formation of $Cu_{1.5}Mn_{1.5}O_4$ spinel phase, which can be due to improved redox properties of these Cu-MnO_x catalysts under CO thanks to copper active centres on the catalyst surface. It is also suggested that the reaction mechanism might be Mars van Krevelen mechanism, which adsorbed CO reacts with active labile oxygen species in the lattice of the catalysts, followed reoxidation of catalysts with molecular oxygen in reaction mixture. Stability test shows that Cu-doped catalyst suffers a relatively severe deactivation, although it is mainly linked to the Cu-doped Mn_2O_3 and cryptomelane phase, while pure cryptomelane and $Cu_{1.5}Mn_{1.5}O_4$ exhibit an excellent stability under real operation conditions.

CRediT authorship contribution statement

Huiyan Pan: Investigation, Writing – review & editing. **Xiaowei Chen:** Conceptualization, Methodology, Investigation, Funding acquisition, Project administration, Writing – original draft. **Carlos Lopez:** Formal analysis, Writing – review & editing. **Javier Martínez-López:** Formal analysis. **Enqi Bu:** Investigation. **Juan J. Delgado:** Conceptualization, Methodology, Investigation, Writing – review & editing, Funding acquisition, Project administration.

Declaration of Competing Interest

The authors declare that they have no known competing financial interests or personal relationships that could have appeared to influence the work reported in this paper.

Data availability

Data will be made available on request.

Acknowledgement

This research was funded by the Ministry of Science, Innovation and Universities of Spain (PID2020-113809RB-C33) and the Junta de Andalucía in Spain (PY18-2727). H. Pan received financial support from the Chinese Scholarship Council for her Ph.D. study at the University of Cadiz, and the Science and Technology Bureau of Nanyang City, China (JCQY012). E. Bu also received support from the University of Cadiz (FPI-UCA grant UCA/R93REC/2019). J. J. Delgado and X. Chen thank the financial support from the IMEYMAT Project at the University of Cadiz, Spain.

Appendix A. Supporting information

Supplementary data associated with this article can be found in the online version at doi:10.1016/j.cattod.2023.114085.

References

[1] H.J. Freund, G. Meijer, M. Scheffler, R. Schlögl, M. Wolf, CO oxidation as a prototypical reaction for heterogeneous processes, Angew. Chem. Int. Ed. 50 (2011) 10064–10094, https://doi.org/10.1002/anie.201101378.
[2] N.K. Soliman, Factors affecting CO oxidation reaction over nanosized materials: a review, J. Mater. Res. Technol. 8 (2019) 2395–2407, https://doi.org/10.1016/j.jmrt.2018.12.012.
[3] A.B. Lamb, W.C. Bray, J.C.W. Frazer, The removal of carbon monoxide from air, J. Ind. Eng. Chem. 12 (1920) 213–221, https://doi.org/10.1021/ie50123a007.
[4] G.J. Hutchings, A.A. Mirzaei, R.W. Joyner, M.R.H. Siddiqui, S.H. Taylor, Effect of preparation conditions on the catalytic performance of copper manganese oxide catalysts for CO oxidation, Appl. Catal. A Gen. 166 (1998) 143–152, https://doi.org/10.1016/S0926-860X(97)00248-2.
[5] S.A. Kondrat, T.E. Davies, Z. Zu, P. Boldrin, J.K. Bartley, A.F. Carley, S.H. Taylor, M.J. Rosseinsky, G.J. Hutchings, The effect of heat treatment on phase formation of copper manganese oxide: influence on catalytic activity for ambient temperature carbon monoxide oxidation, J. Catal. 281 (2011) 279–289, https://doi.org/10.1016/j.jcat.2011.05.012.
[6] R. Yousef, A. Al-zoubi, N. Sad-din, A study of structural properties of $CuMn_2O_4$ synthesized by solid state method, Adv. Phys. Theor. Appl. 71 (2018) 24–30.
[7] D. Fang, J. Xie, D. Mei, Y. Zhang, F. He, Effect of $CuMn_2O_4$ spinel in Cu – Mn oxide catalysts on selective catalytic reduction of NO_x with NH_3 at low temperature, RSC Adv. 4 (2014) 25540–25551, https://doi.org/10.1039/c4ra02824d.
[8] P. Wei, M. Bieringer, L.M.D. Cranswick, A. Petric, In situ high-temperature X-ray and neutron diffraction of Cu–Mn oxide phases, J. Mater. Sci. 45 (2010) 1056–1064, https://doi.org/10.1007/s10853-009-4042-2.
[9] S. Behar, P. Gonzalez, P. Agulhon, F. Quignard, D. Świerczyński, New synthesis of nanosized Cu-Mn spinels as efficient oxidation catalysts, Catal. Today 189 (2012) 35–41, https://doi.org/10.1016/j.cattod.2012.04.004.
[10] S. Joshi, A. Petric, Nickel substituted $CuMn_2O_4$ spinel coatings for solid oxide fuel cell interconnects, Int. J. Hydrog. Energy 42 (2016) 5584–5589, https://doi.org/10.1016/j.ijhydene.2016.08.075.
[11] T.J. Clarke, T.E. Davies, S.A. Kondrat, S.H. Taylor, Mechanochemical synthesis of copper manganese oxide for the ambient temperature oxidation of carbon monoxide, Appl. Catal. B Environ. 165 (2015) 222–231, https://doi.org/10.1016/j.apcatb.2014.09.070.
[12] T. Liu, Y. Yao, L. Wei, Z. Shi, L. Han, H. Yuan, B. Li, L. Dong, F. Wang, C. Sun, Preparation and evaluation of copper-manganese oxide as a high-efficiency catalyst for CO oxidation and NO reduction by CO, J. Phys. Chem. C 121 (2017) 12757–12770, https://doi.org/10.1021/acs.jpcc.7b02052.
[13] K. Wegner, M. Medicus, E. Schade, J. Grothe, S. Kaskel, Tailoring catalytic properties of copper manganese oxide nanoparticles (Hopcalites-2G) via flame spray pyrolysis, ChemCatChem 10 (2018) 3914–3922, https://doi.org/10.1002/cctc.201800639.
[14] Y.G. Yin, W.Q. Xu, S.L. Suib, C.L. O'Young, Lattice oxygen mobility and structural stability of Ni and Cu octahedral molecular sieves having the cryptomelane structure, Inorg. Chem. 34 (1995) 4187–4193, https://doi.org/10.1021/ic00120a025.
[15] E. Nicolas-Tolentino, Z.-R. Tian, H. Zhou, G. Xia, S.L. Suib, Effects of Cu^{2+} ions on the structure and reactivity of todorokite- and cryptomelane-type manganese oxide octahedral molecular sieves, Chem. Mater. 11 (1999) 1733–1741, https://doi.org/10.1021/cm9811040.
[16] M. Sun, L. Yu, F. Ye, G. Diao, Q. Yu, Z. Hao, Y. Zheng, L. Yuan, Transition metal doped cryptomelane-type manganese oxide for low-temperature catalytic combustion of dimethyl ether, Chem. Eng. J. 220 (2013) 320–327, https://doi.org/10.1016/j.cej.2013.01.061.
[17] I. Gómez-Recio, H. Pan, A. Azor-Lafarga, M.L. Ruiz-González, M. Hernando, M. Parras, M.T. Fernández-Díaz, J.J. Delgado, X. Chen, D.G. Jiménez, D. Portehault, C. Sanchez, M. Cabero, A. Martínez-Arias, J.M. González-Calbet, J. J. Calvino, Exceptional low-temperature CO oxidation over noble-metal-free iron-doped hollandites: an in-depth analysis of the influence of the defect structure on catalytic performance, ACS Catal. 11 (2021) 15026–15039, https://doi.org/10.1021/acscatal.1c04954.
[18] X. Wang, W. Tan, K. Guo, J. Ji, F. Gao, Q. Tong, L. Dong, Evaluation of manganese oxide octahedral molecular sieves for CO and C_3H_6 oxidation at diesel exhaust

conditions, Front. Environ. Chem. 2 (2021) 1–11, https://doi.org/10.3389/fenvc.2021.672250.
[19] J. Bao, X. Duan, P. Zhang, Facile synthesis of a $CuMnO_X$ catalyst based on a mechanochemical redox process for efficient and stable CO oxidation, J. Mater. Chem. A 8 (2020) 24438–24444, https://doi.org/10.1039/d0ta07304k.
[20] Z. Fu, M. Chen, Q. Ye, N. Dong, H. Dai, Enhanced performance of the OMS-2-supported CuO_x catalysts for carbon monoxide, ethyl acetate, and toluene oxidation, Catalysts 11 (2021) 713, https://doi.org/10.3390/catal11060713.
[21] H. Pan, X. Chen, O. Sanz, M.A. Cauqui, J.M. Rodríguez-Izquierdo, J.J. Delgado, A facile one-pot hydrothermal synthesis as an efficient method to modulate the potassium content of cryptomelane and its effects on the redox and catalytic properties, Chin. J. Catal. 40 (2019) 940–952, https://doi.org/10.1016/S1872-2067(19)63339-5.
[22] X. Chen, Y.F. Shen, S.L. Suib, C.L. O'Young, Characterization of manganese oxide octahedral molecular sieve (M-OMS-2) materials with different metal cation dopants, Chem. Mater. 14 (2002) 940–948, https://doi.org/10.1021/cm000868o.
[23] R.D. Shannon, Revised effective ionic radii and systematic studies of interatomie distances in halides and chaleogenides, Acta Cryst. A32 (1976) 751–766.
[24] Y.-G. Yin, W.-Q. Xu, R. DeGuzman, S.L. Suib, Studies of stability and reactivity of synthetic cryptomelane-like manganese oxide octahedral molecular sieves, Inorg. Chem. 33 (1994) 4384–4389, https://doi.org/10.1021/ic00097a029..
[25] C.K. King'ondu, N. Opembe, C. Chen, K. Ngala, H. Huang, A. Iyer, H.F. Garcés, S. L. Suib, Manganese oxide octahedral molecular sieves (OMS-2) multiple framework substitutions: a new route to OMS-2 particle size and morphology control, Adv. Funct. Mater. 21 (2011) 312–323, https://doi.org/10.1002/adfm.201001020.
[26] R. Kumar, J. Mittal, N. Kushwaha, B.V. Rao, S. Pandey, C.P. Liu, Room temperature carbon monoxide gas sensor using Cu doped OMS-2 nanofibers, Sens. Actuators B Chem. 266 (2018) 751–760, https://doi.org/10.1016/j.snb.2018.03.182.
[27] A. Awaluddin, L. Astuti, A. Linggawati, S.S. Siregar, P. Prasetya, L. Saputra, The Cu-doped cryptomelane-type octahedral molecular sieve manganese oxide synthesized by sol-gel for the degradation of methylene blue, AIP Conf. Proc., 2026 (2018) 020075. https://doi.org/10.1063/1.5065035.
[28] R. Jothiramalingam, B. Viswanathan, T.K. Varadarajan, Synthesis and structural characterization of copper incorporated manganese oxide OMS-2 materials synthesized via potassium birnessite, Mater. Chem. Phys. 100 (2006) 257–261, https://doi.org/10.1016/j.matchemphys.2005.12.040.
[29] M. Thommes, K. Kaneko, V.A. Neimark, J.P. Olivier, F. Rodriguez-Reinoso, J. Rouquerol, K.S.W. Sing, Physisorption of gases, with special reference to the evaluation of surface area and pore size distribution (IUPAC Technical Report, Pure Appl. Chem. 0 (2015) 1051–1069, https://doi.org/10.1515/pac-2014-1117.
[30] H. Kurata, C. Colliex, Electron-energy-loss core-edge structures in manganese oxides, Phys. Rev. B 48 (1993) 2102–2108, https://doi.org/10.1103/PhysRevB.48.2102.
[31] F.M.F. de Groot, M. Grioni, J.C. Fuggle, Oxygen 1s x-ray-absorption edges of transition-metal oxides,, Phys. Rev. B 40 (1989) 5715–5723. https://doi.org/10.1103/PhysRevB.40.5715.
[32] S. Zhang, K.J.T. Livi, A.C. Gaillot, A.T. Stone, D.R. Veblen, Determination of manganese valence states in (Mn^{3+}, Mn^{4+}) minerals by electron energy-loss spectroscopy, Am. Mineral. 95 (2010) 1741–1746, https://doi.org/10.2138/am.2010.3468.
[33] L.A.J. Garvie, A.J. Craven, High-resolution parallel electron energy-loss spectroscopy of Mn $L_{2,3}$-edges in inorganic manganese compounds, Phys. Chem. Miner. 21 (1994) 191–206, https://doi.org/10.1007/BF00202132.
[34] V.J. Keast, Application of EELS in materials science, Mater. Charact. 73 (2012) 1–7, https://doi.org/10.1016/j.matchar.2012.07.013.
[35] W.B. Li, Z.X. Liu, R.F. Liu, J.L. Chen, B.Q. Xu, Rod-like $CuMnO_x$ transformed from mixed oxide particles by alkaline hydrothermal treatment as a novel catalyst for catalytic combustion of toluene, Phys. Chem. Chem. Phys. 18 (2016) 22794–22798, https://doi.org/10.1039/c6cp03433k.
[36] J. Wang, J. Chen, L. Peng, H. Zhang, Z. Jiang, K. Xiong, Q. Yang, J. Chen, N. Yang, On the CuO-Mn_2O_3 oxide-pair in $CuMnO_x$ multi-oxide complexes: structural and catalytic studies, Appl. Surf. Sci. 575 (2022), 151733, https://doi.org/10.1016/j.apsusc.2021.151733.
[37] A. Raja, R. Rajendiran, D. Chinnadurai, K. Prabakar, Stabilization of cryptomelane α-MnO_2 nanowires tunnels widths for enhanced electrochemical energy storage, Electrochim. Acta 283 (2018) 1679–1688, https://doi.org/10.1016/j.electacta.2018.07.095.
[38] M.R. Morales, B.P. Barbero, L.E. Cadús, Total oxidation of ethanol and propane over Mn-Cu mixed oxide catalysts, Appl. Catal. B Environ. 67 (2006) 229–236, https://doi.org/10.1016/j.apcatb.2006.05.006.
[39] M. Özacar, A.S. Poyraz, H.C. Genuino, C.H. Kuo, Y. Meng, S.L. Suib, Influence of silver on the catalytic properties of the cryptomelane and Ag-hollandite types manganese oxides OMS-2 in the low-temperature CO oxidation, Appl. Catal. A Gen. 462–463 (2013) 64–474,, https://doi.org/10.1016/j.apcata.2013.04.027.
[40] W.Y. Hernández, M.A. Centeno, S. Ivanova, P. Eloy, E.M. Gaigneaux, J. A. Odriozola, Cu-modified cryptomelane oxide as active catalyst for CO oxidation reactions, Appl. Catal. B Environ. 123–124 (2012) 27–35, https://doi.org/10.1016/j.apcatb.2012.04.024.
[41] B. Liu, H. Wu, S. Li, M. Xu, Y. Cao, Y. Li, Solid-state construction of CuO_x/$Cu_{1.5}Mn_{1.5}O_4$ nanocomposite with abundant surface CuO_x species and oxygen vacancies to promote CO oxidation activity, Int. J. Mol. Sci. 23 (2022) 6856, https://doi.org/10.3390/ijms23126856.
[42] B.E. Martin, A. Petric, Electrical properties of copper – manganese spinel solutions and their cation valence and cation distribution, J. Phys. Chem. Solids 68 (2007) 2262–2270, https://doi.org/10.1016/j.jpcs.2007.06.019.
[43] G.G. Xia, Y.G. Yin, W.S. Willis, J.Y. Wang, S.L. Suib, Efficient stable catalysts for low temperature carbon monoxide oxidation, J. Catal. 185 (1999) 91–105, https://doi.org/10.1006/jcat.1999.2484.
[44] K. Ramesh, L. Chen, F. Chen, Y. Liu, Z. Wang, Y.-F. Han, Re-investigating the CO oxidation mechanism over unsupported MnO, Mn_2O_3 and MnO_2 catalysts, Catal. Today 131 (2008) 477–482, https://doi.org/10.1016/j.cattod.2007.10.061.
[45] C. Jones, K.J. Cole, S.H. Taylor, M.J. Crudace, G.J. Hutchings, Copper manganese oxide catalysts for ambient temperature carbon monoxide oxidation: effect of calcination on activity, J. Mol. Catal. A Chem. 305 (2009) 121–124, https://doi.org/10.1016/j.molcata.2008.10.027.
[46] K. Morgan, K.J. Cole, A. Goguet, C. Hardacre, G.J. Hutchings, N. Maguire, S. O. Shekhtman, S.H. Taylor, TAP studies of CO oxidation over $CuMnO_X$ and Au/$CuMnO_X$ catalysts, J. Catal. 276 (2010) 38–48, https://doi.org/10.1016/j.jcat.2010.08.013.
[47] X.S. Liu, Z.N. Jin, J.Q. Lu, X.X. Wang, M.F. Luo, Highly active CuO/OMS-2 catalysts for low-temperature CO oxidation, Chem. Eng. J. 162 (2010) 151–157, https://doi.org/10.1016/j.cej.2010.05.015.
[48] V.P. Santos, M.F.R. Pereira, J.J.M. Órfão, J.L. Figueiredo, The role of lattice oxygen on the activity of manganese oxides towards the oxidation of volatile organic compounds, Appl. Catal. B Environ. 99 (2010) 353–363, https://doi.org/10.1016/j.apcatb.2010.07.007.
[49] S.A.C. Carabineiro, V.P. Santos, M.F.R. Pereira, J.J.M. Órfão, J.L. Figueiredo, CO oxidation over gold supported on Cs, Li and Ti-doped cryptomelanematerials, J. Colloid Interface Sci. 480 (2016) 17–29. https://doi.org/10.1016/j.jcis.2016.06.072.
[50] V.P. Santos, S.A.C. Carabineiro, J.J.W. Bakker, O.S.G.P. Soares, X. Chen, M.F. R. Pereira, J.J.M. Órfão, J.L. Figueiredo, J. Gascon, F. Kapteijn, Stabilized gold on cerium-modified cryptomelane: Highly activein low-temperature CO oxidation, J. Catal. 309 (2014) 58–65. https://doi.org/10.1016/j.jcat.2013.08.030.